First-principles local-stress calculations for oxygen vacancies in silicon oxide glass materials

Koshin Maekawa,[1] Takumu Ito,[1] Tomoyuki Tamura,[1,*] Shingo Tanaka,[2] Masanori Kohyama,[2] and Assil Bouzid[3]

[1]*Division of Applied Physics, Nagoya Institute of Technology, Nagoya, Aichi 466-8555, Japan*

[2]*Research Institute of Electrochemical Energy, Department of Energy and Environment, National Institute of Advanced Industrial Science and Technology (AIST), Ikeda, Osaka 563-8577, Japan*

[3]*Institut de Recherche sur les Céramiques (IRCER), UMR CNRS 7315, F-87068 Université de Limoges, Centre Européen de la Céramique, 12 rue Atlantis, Limoges, France*

(Received 30 July 2025; revised 3 October 2025; accepted 17 October 2025; published 6 November 2025)

We systematically investigated the correlation between defect formation energy and local stress states in amorphous SiO_2 (a-SiO_2) using first-principles calculations within density functional theory. Although conventional approaches require the structural relaxation of oxygen vacancy at each site, we demonstrated that the formation tendency of oxygen vacancies can be quantitatively predicted from the local stress state in a nondefective system. To achieve this, we employed a real-space analysis based on Bader partitioning and introduced a unit-based averaging method for local structural units, enabling physically meaningful stress evaluations in ionically disordered systems. A strong statistical correlation was found between the formation energy and the unit-averaged stress in the Si–O–Si unit, suggesting that the local compressive environments significantly facilitated oxygen removal with large structural relaxation. These results establish a predictive framework for identifying defect-prone sites in disordered systems, including amorphous structures, without exhaustive defect structure generation, thereby offering an efficient route for defect analysis and material design.

DOI: 10.1103/pm9m-n49m

I. INTRODUCTION

Amorphous silicon dioxide (a-SiO_2) is an important material for various technical applications, including electronic and optoelectronic devices and optical communication fibers. Various structural defects in a-SiO_2 affect its optical transparency and reduce device performance [1,2]. In a-SiO_2, SiO_4 tetrahedra share corners to form a glass network and disorder is classified into two types [3]. The first is a short-range chemical disorder, which is different from SiO_4 tetrahedra, such as oxygen defects, Si defects, and impurities. Oxygen vacancies are a type of chemical disorder known to cause an optical absorption band around 7.6 eV due to Si–Si bonds [4,5]. These vacancies are extremely important defects because they can be transformed into various species of defects by high-energy laser irradiation, resulting in new optical absorption bands [6,7]. The second is a middle-range physical disorder, such as the distribution of Si–O–Si bond angles and $(Si–O)_n$ ring structures. Previous studies on isolated disiloxane molecules (SiH_3–O–SiH_3) have shown that the Si–O–Si bending potential is very flat, with a barrier of only a few kcal/mol between a bent ($\sim$140°) and a linear configuration [8,9]. This indicates the intrinsic flexibility of the Si–O–Si angle, which underlies the wide bond-angle distribution observed in the glassy network, although the effective potential in solids is further modified by network constraints.

Most previous theoretical studies have focused on single point-defect structures and there is a lack of understanding of the relationship between physical disorder and defect properties. In a recent study [10] based on first-principles calculations, a linear relationship between the formation energy of oxygen vacancies and the Si–Si bond distance was clarified and the relationship between structural disorder, defect levels, and optical absorption properties was systematically evaluated. However, in first-principles calculations of the formation energy of an oxygen vacancy, the process of removing an oxygen atom and relaxing the atomic configuration must be performed for each oxygen atom, which incurs a high computational cost.

Currently, first-principles computational codes based on density functional theory (DFT) with a plane-wave basis, such as VASP [11,12], CASTEP [13], ABINIT [14], and QUANTUM ESPRESSO [15,16], are widely used. Using these DFT codes, we can obtain the total energy and stress tensor as quantities integrated or averaged in a supercell. However, we cannot obtain any local distribution of energy or stress inside a supercell. If these can be obtained for a large supercell containing a defect, our understanding of the nature of the defect can be greatly improved. Thus practical computational techniques to obtain the local energy and stress inside a supercell have been developed [17,18] in the framework of the generalized gradient approximation (GGA) [19] and projector augmented-wave (PAW) method [12,20] and these have been implemented in the QMAS (Quantum Materials Simulator) code [21]. The local energy and stress are calculated by integrating the energy and stress densities in each selected local region to settle the gauge-dependent problem. These techniques are extensions of the original energy– and stress–density schemes [22,23] and they have been applied to various problems involving surfaces

*Contact author: tamura.tomoyuki@nitech.ac.jp

and grain boundaries in metals and Si [24]. Atomic energy calculations have also been conducted for machine learning, not only for coincident grain boundaries [25] but also for random grain boundaries [26]. However, the application of local energy and stress calculations to oxides that exhibit charge transfer through bonds has not been thoroughly studied.

Considering oxide applications, the effect of charge transfer on local energy and stress should be investigated, although there exists inherent ambiguity in defining a transfer value associated with a locally defined region, which seems to more seriously affect the local energy as an extensive quantity than the local stress as an intensive quantity. It should be noted that a large amount of electrons in a defined local region by charge transfer naturally leads to a larger magnitude of a negative local energy value, while this cannot be regarded simply as a sign of the stability of such a site because of the nature of an extensive quantity, as discussed in Ref. [24]. Even for the atomic stresses in the present framework, it is known that anionic and cationic atoms show compressive and tensile stresses, respectively, owing to charge transfer in oxides or ionic crystals, whereas the volume average of such atomic stresses is zero in typical crystals. Therefore, the physical meaning of the atomic stress within each ionic site is unclear. It is desirable to develop new analysis schemes for the local energy and stress in ionic solids, compounds, or alloys with substantial charge transfer, where the sum or average of the neighboring ionic pairs or clusters might be more effective than analyzing each value of the cationic or anionic atoms.

In this study, we clarify the correlation between the defect formation energies and local stresses in the atomic arrangement of nondefective a-SiO_2. To expand the application scope of first-principles local stress calculations, which have been applied mainly to metal systems, to oxides, we use the average values of clusters of adjacent atoms. This makes it possible to obtain physically meaningful local stress distributions that cannot be observed experimentally. Such stress distributions can also be visualized.

II. METHODS

An a-SiO_2 model was generated using classical molecular dynamics (MD) simulations with the DL_POLY code [27]. A cubic cell containing 192 atoms was used. The melting–cooling process started with a random atomic arrangement. The system was held at 2000 K for 200 ps in the *NVT* ensemble using the Nosé–Hoover thermostat [28] and cooled to 1 K at a rate of 1 K/ps in the *NVT* ensemble. Morse-type potentials parametrized in Ref. [29] were used for two-body interatomic interactions. The interaction cutoff was set to 6 Å. The MD time step was 1.0 fs.

For the cell model obtained by classical MD, isotropic cell relaxation was performed using the first-principles QMAS code [21] such that the hydrostatic pressure was approximately 0 GPa. Electronic exchange-correlation interactions were evaluated using the GGA formulated by Perdew, Burke, and Ernzerhof (PBE) [19]. Electron–core interactions were described using the PAW pseudopotentials [12,20]. The plane-wave energy cutoff was set to 476 eV (=35 Ry) and the k-point grid was set as the Γ point. Figure 1 shows a relaxed a-SiO_2 configuration obtained via first-principles calculations.

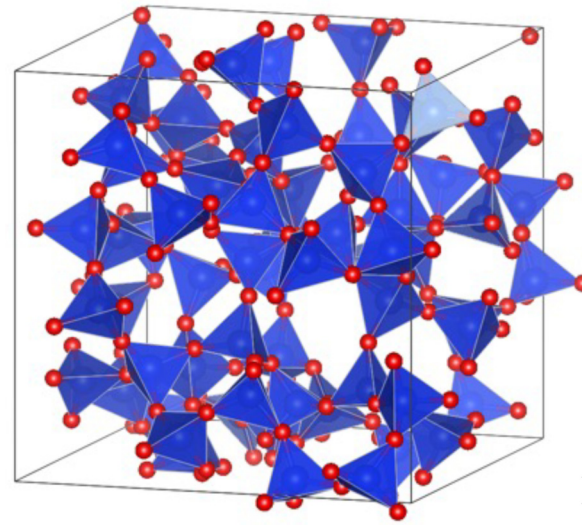

FIG. 1. Amorphous SiO_2 configuration generated by the melting–cooling process through classical MD and relaxed using the first-principles method, which consists of 64 Si atoms (blue) and 128 O atoms (red). The cubic-cell dimensions are 14.07 Å.

The length of each side of the cubic cell was 14.07 Å and the density was 2.30 g/cm^3.

In plane-wave DFT calculations, the total energy and stress tensor are obtained as integrated quantities of the entire system, respectively. There is no universal or generally accepted method for partitioning a supercell into local regions. Among several schemes for partitioning space, Bader method, which divides space into atomic regions according to the gradient of the electron density using zero-flux surfaces as boundaries, offers a natural and practical means of obtaining local distributions in a consistent manner. This assigns electrons and volumes to individual atoms in a basis-set–independent way. Bader charges are widely employed to evaluate charge transfer. In this study, we applied the Bader partitioning to analyze local energies and stresses. The atomic energy E_i for atom i is obtained by integrating the energy density $\epsilon(\mathbf{r})$ over the Bader region Ω_i of atom i [17,18],

$$E_i = \int_{\Omega_i} \epsilon(\mathbf{r})\, d\mathbf{r}. \tag{1}$$

The energy density suffers from the gauge-dependent problem of the kinetic terms, namely the nonuniqueness or ambiguity for the choice of symmetric or asymmetric forms of the kinetic terms. Gauge-independent atomic energies can be obtained in such a Bader region, because the gauge-dependent term in the kinetic energy density is integrated to zero. The energy density $\epsilon(\mathbf{r})$ is a real-space integrant function of the total energy and the integration over the full supercell corresponds to the conventional total energy. Thus the atomic energy is the decomposition of the conventional total energy of a supercell into its constituent atoms, according to the Bader partitioning of the charge density distribution in a supercell:

$$E_{\mathrm{cell}}(N) = \int_{\Omega} \epsilon(\mathbf{r})\, d\mathbf{r} = \sum_{i=1}^{N} E_i, \tag{2}$$

where N is the number of atoms and $\Omega = \sum_i \Omega_i$ is the total cell volume.

The stress density $\tau_{\alpha\beta}(\mathbf{r})$ is a real-space integrant function and a local stress of atom i is given by its integration in a local region of atom i, divided by its volume Ω_i as

$$\sigma^i_{\alpha\beta} = \frac{1}{\Omega_i}\int_{\Omega_i} \tau_{\alpha\beta}(\mathbf{r})\, d\mathbf{r}, \tag{3}$$

ensuring the nature of an intensive quantity. Then, the stress tensor $\sigma_{\alpha\beta}$ of a full supercell is expressed as follows:

$$\sigma_{\alpha\beta} = \frac{1}{\Omega}\frac{\partial E_{\text{tot}}}{\partial \varepsilon_{\alpha\beta}} = \frac{1}{\Omega}\int_{\Omega} \tau_{\alpha\beta}(\mathbf{r})\, d\mathbf{r} = \frac{1}{\Omega}\sum_i \Omega_i \sigma^i_{\alpha\beta}, \tag{4}$$

where $\sigma_{\alpha\beta}$ and $\varepsilon_{\alpha\beta}$ are the stress tensor and strain tensor for the supercell, respectively, with a volume of $\Omega = \sum_i \Omega_i$. By using the same Bader partitioning as the local energy, the gauge-dependent terms in the kinetic-stress density can be integrated to be zero in each Bader region only for the diagonal sum as $\tau_{11} + \tau_{22} + \tau_{33}$ [17,24]. Thus we only obtain the diagonal sum $\sigma^i_{11} + \sigma^i_{22} + \sigma^i_{33}$ as a local stress of atom i without the gauge-dependent problem, which is simple hydrostatic compression or tension.

The energy and stress densities were computed on fast Fourier transform (FFT) mesh grids within the PAW–GGA framework. The Bader integration of the energy and stress density was performed using the Yu–Trinkle algorithm [30]. Positive stress values indicate tension, while negative stress values indicate compression.

III. RESULTS AND DISCUSSION

Figure 2 shows the Bader volumes and charges of Si and O in a-SiO_2. For comparison, values for α-quartz and stishovite SiO_2 are also shown. The Bader volume and charge of O are significantly larger than those of Si due to electronegativity differences, leading to charge transfer from Si to O. The Bader volumes are larger in amorphous forms than in crystalline phases due to lower density and larger voids. The Bader charge of four-coordinated Si in α-quartz is larger than that of six-coordinated Si in stishovite and the Bader charge of two-coordinated O in α-quartz is smaller than that of three-coordinated O in stishovite. This indicates that stishovite has more charge transfer from Si to O than α-quartz and exhibits stronger ionic bonds. This tendency is consistent with the result that the absolute values of Born effective charges increase with increasing coordination number of cation ions [31]. However, the width of the Bader charge distribution in a-SiO_2 is greater than the difference between α-quartz and stishovite.

Figure 3 shows the atomic energies and stresses of Si and O in a-SiO_2. Both the atomic energy and the atomic stress are close to those of α-quartz. This is because the local environment, including the coordination number of Si and O in a-SiO_2, is similar to that of α-quartz. It is important to note that while there is a large distribution of the Bader volume and Bader charge, as shown in Fig. 2, the distribution widths of the atomic energy and atomic stress are small. Atomic stress is tensile in Si and compressive in O. The atomic stress can be considered as a response to the virtual expansion or compression of each Bader region. When the charge transfer from cation to anion becomes large, such as from α-quartz to stishovite, stronger tensile and compressive stresses are generated. From these results, the atomic energy and stress seem to represent the atomic environment, but it is not easy to obtain a clear physical picture of the local energy and stress using only the atomic values of each anionic and cationic atom, as discussed in Sec. I.

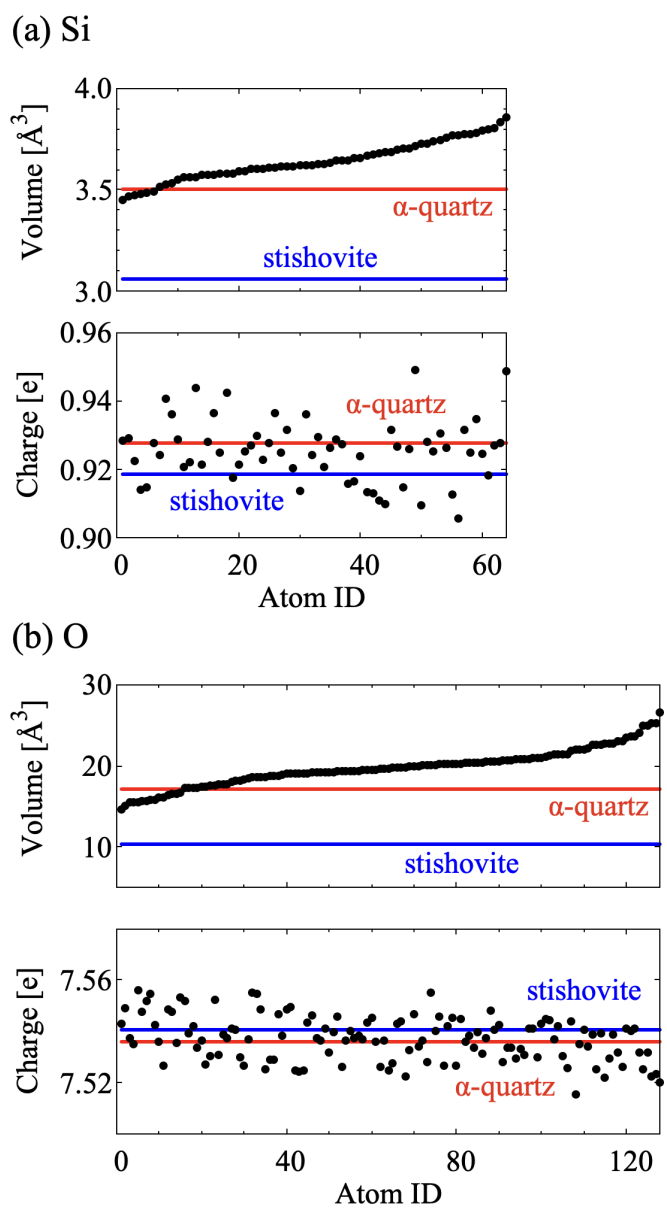

FIG. 2. Bader volume and Bader charge for (a) Si and (b) O in a-SiO_2 compared to α-quartz and stishovite SiO_2.

In addition to atomic stresses as the response of each Bader region, we should examine the response of interatomic bonds or atomic rings to virtual compression or expansion to clarify the local stress features of the bonding network in a-SiO_2. Therefore, we considered that using a charge-neutral atomic cluster as the analytical unit would better reflect bonding or ring network effects than using individual atoms. We introduced the unit-averaged hydrostatic pressure. In the case of

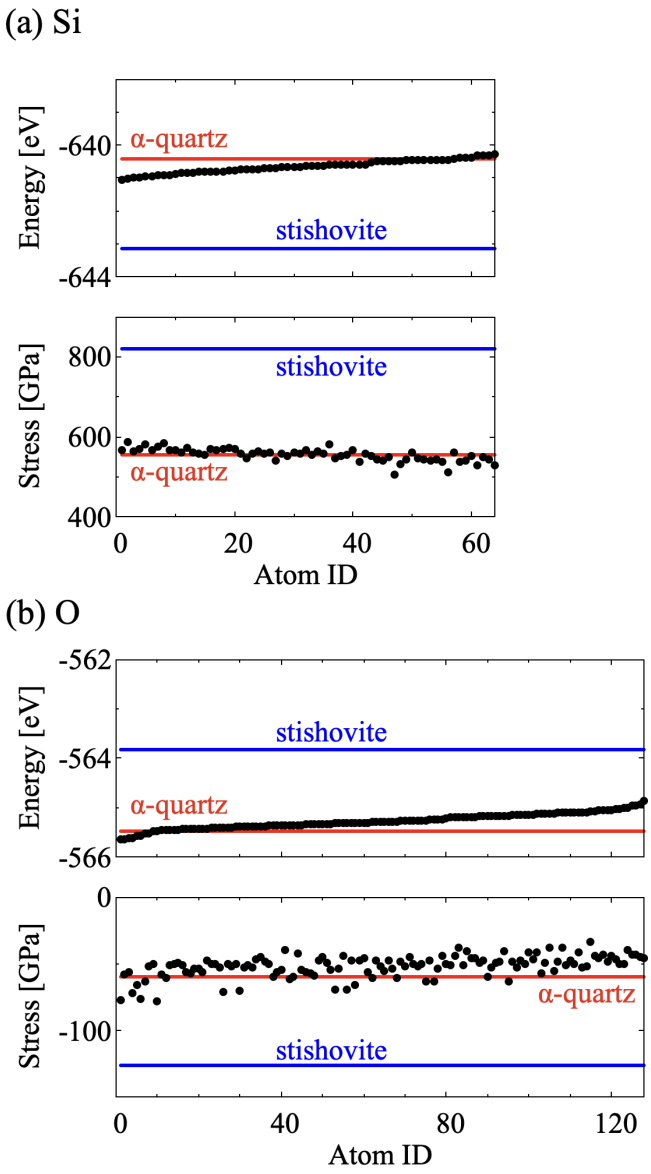

FIG. 3. Atomic energy and atomic stress for (a) Si and (b) O in a-SiO_2 compared to α-quartz and stishovite SiO_2.

a-SiO_2, the smallest units were the $Si_{1/2}O$ unit in the Si–O–Si bond and the SiO_2 unit in the SiO_4 tetrahedron. The unit averaged Si–O–Si stress can be defined as the average stress of the central O atom and two adjacent Si atoms as follows:

$$\tilde{\sigma}_i^{\mathrm{O}} = \frac{\Omega_i^{\mathrm{O}}\sigma_i^{\mathrm{O}} + \frac{1}{4}\sum_j^2 \Omega_j^{\mathrm{Si}}\sigma_j^{\mathrm{Si}}}{\Omega_i^{\mathrm{O}} + \frac{1}{4}\sum_j^2 \Omega_j^{\mathrm{Si}}}, \tag{5}$$

where the contribution of four-coordinated Si to the Si–O–Si unit is 1/4. The unit-averaged stress of a SiO_4 tetrahedron can be defined as the average stress of the central Si atom and four adjacent O atoms as follows:

$$\tilde{\sigma}_i^{\mathrm{Si}} = \frac{\Omega_i^{\mathrm{Si}}\sigma_i^{\mathrm{Si}} + \frac{1}{2}\sum_j^4 \Omega_j^{\mathrm{O}}\sigma_j^{\mathrm{O}}}{\Omega_i^{\mathrm{Si}} + \frac{1}{2}\sum_j^4 \Omega_j^{\mathrm{O}}}, \tag{6}$$

where the contribution of two-coordinated O to the SiO_4 tetrahedron is 1/2. The average stress of the Si–O–Si and SiO_4 tetrahedral units is zero in the case of a crystal structure with

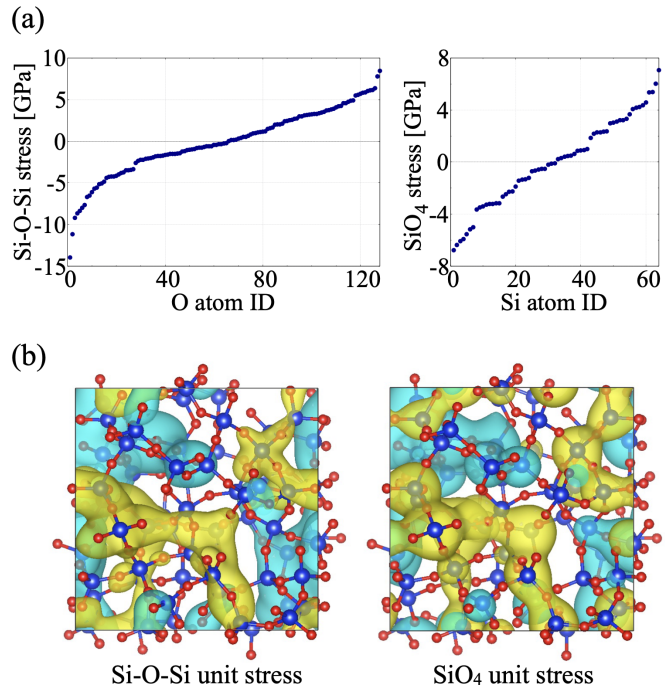

FIG. 4. Distribution of the unit averaged stresses of Si-O-Si bond and SiO4 tetrahedron in a-SiO_2 (a) and plots of those systems using three-dimensional Gaussian functions (b). Tensile regions are shown in yellow and compressed regions are shown in blue.

stable lattice constants, whereas both positive and negative local stresses occur in such structural units, reflecting the short- or intermediate-range structural disorder within an amorphous structure.

Figure 4 shows the distribution of the unit-averaged stress of the Si–O–Si unit and the SiO_4 tetrahedron in a-SiO_2. The hydrostatic pressure was almost zero throughout the cell using Eq. (4); however, the unit average stresses exhibited both tension and compression. Figure 4(b) shows the unit-averaged stress of the Si–O–Si unit and the SiO_4 tetrahedron. A stress value was assigned to the center of each unit, O or Si, and then the values were smeared using three-dimensional Gaussian functions of $\sigma = 0.5$ Å and summed. The tensile regions are shown in the yellow and the compressed regions in the blue. The distributions of the tensile and compressive regions were similar in the Si–O–Si unit and SiO_4 tetrahedron.

The formation energy of the neutral oxygen vacancy can be obtained as

$$E_{\mathrm{form}} = E_{\mathrm{T}}(\mathrm{Si_{64}O_{127}}) - E_{\mathrm{T}}(\mathrm{Si_{64}O_{128}}) + \mu_{\mathrm{O}}, \tag{7}$$

where E_{T} is the total energy of the supercell. μ_{O} is the atomic chemical potential of oxygen and is defined to vary between the oxygen-rich and oxygen-poor limits. As in previous studies [10,32], the formation energies were calculated under the oxygen-rich condition, where μ_{O} was taken as half of the total energy of the O_2 molecule. In the oxygen-poor limit, the formation energies decreased uniformly by 4.11 eV. To calculate the formation energy of oxygen vacancies, it is necessary to generate an initial configuration by removing oxygen and perform structural relaxation for each vacancy. For an amorphous model, it is necessary to perform

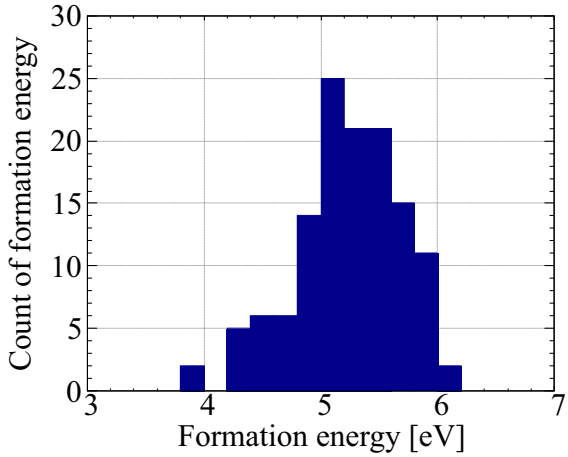

FIG. 5. Histogram of the count of formation energy.

the above procedure for oxygen atoms in the supercell and the computational cost is much higher. We also calculated the formation energy in α-quartz SiO_2 as 5.31 eV under the same condition.

The mean formation energy was 5.23 eV for 128 oxygen vacancy sites, which is similar to 5.31 eV for α-quartz, 5.23 eV for 64 oxygen vacancy sites [10], and the values in previous DFT calculations [32]. Figure 5 shows the distribution of formation energies of the oxygen vacancies. It is shown that the formation energies range from 3.87 to 6.17 eV with a central value of 5.23 eV. A previous study reported a range from 4.4 to 6 eV with the central values of 4.4–4.8 and 5.2–5.6 eV [10]. The variation in the formation energies was due to local structural disorder within the amorphous structure and the distribution of the local structural disorder strictly depended on the model.

Figure 6 shows the statistical correlation between the formation energy of the oxygen vacancies and the Si–Si distance before and after oxygen removal. The correlation between the Si–Si distance before oxygen removal and the formation

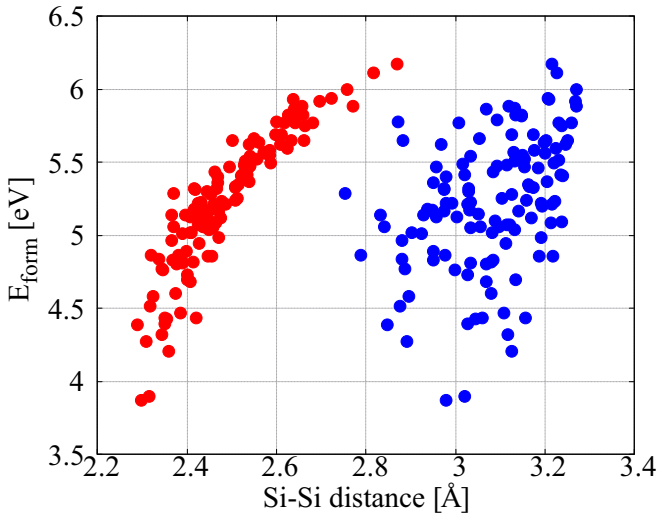

FIG. 6. Formation energy of oxygen vacancies as a function of the Si–Si distance before (blue) and after (red) oxygen removal.

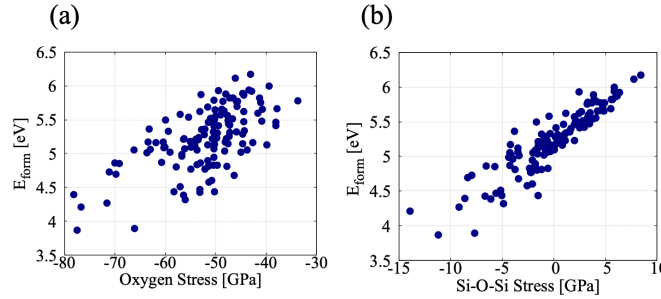

FIG. 7. Formation energy of oxygen vacancies as a function of (a) atomic oxygen stress and (b) Si–O–Si unit stress.

energy was weak. When oxygen vacancies were introduced by oxygen removal, Si–Si bonds formed and the Si–Si distance decreased. The Si–Si distance exhibited a strong correlation with the formation energy, with a correlation coefficient of 0.90. Previous first-principles calculations using a supercell containing 96 atoms showed a linear relationship between the formation energy of oxygen vacancies and the Si–Si bonds after oxygen removal [10]. Our first-principles calculations, using a supercell containing 192 atoms, strongly supported these results. However, it should be emphasized that the Si–Si distance of the oxygen vacancy is obtained after structural relaxation.

Figure 7 shows the statistical correlation between the formation energy of oxygen vacancies and the local stress in the nondefective system. Figure 7(a) shows the correlation between the defect formation energy and the atomic oxygen stress. The higher the compressive stress, the smaller the formation energy. However, the correlation coefficient was 0.63 and a wide distribution was observed. Figure 7(b) shows the correlation between the defect formation energy and Si–O–Si unit stress. Similarly to atomic oxygen stress, there is a tendency for the formation energy to decrease as the compressive stress increases. However, the correlation coefficient was 0.91, indicating a strong correlation. These results demonstrate that oxygen atoms subjected to compressive stress in local Si–O–Si configurations can be easily removed.

We next discuss why the Si–O–Si unit stress can predict the defect formation energy. The defect formation energy can be decomposed into two energies as

$$E_{\text{form}} = E_{\text{rm}}^{\text{fix}}(\text{O}) - E^{\text{relax}}, \tag{8}$$

where $E_{\text{rm}}^{\text{fix}}(\text{O})$ is the energy required to remove an oxygen atom in the oxygen-rich limit while keeping the atomic arrangement of the entire system fixed and E^{relax} is the decrease in energy due to structural relaxation after oxygen removal. The correlation between these energies and the Si–O–Si unit stress is shown in Fig. 8. The slopes of the linear fitting were +0.022 and –0.082 for $E_{\text{rm}}^{\text{fix}}(\text{O})$ and E^{relax}, respectively. Even considering the error in the slope, the absolute value of the slope of E^{relax} is greater than that of $E_{\text{rm}}^{\text{fix}}(\text{O})$. Therefore, the Si–O–Si unit stress can be used as a descriptor to predict the defect formation energy because it can be used to predict the energy decrease due to structural relaxation. As shown in Fig. 6, a shorter Si–Si interatomic distance after structural relaxation results in a smaller defect formation energy. The presence of compressive local stress indicates that

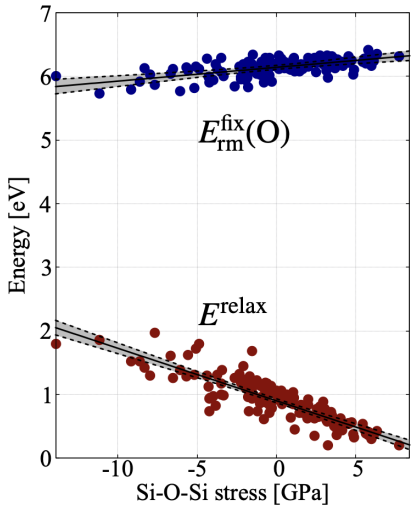

FIG. 8. $E_{\rm rm}^{\rm fix}$(O) and $E^{\rm relax}$ plotted as functions of the Si–O–Si unit stress. The linear fittings are shown together with 95% credible intervals, represented as gray shaded regions. The formation energy of an oxygen vacancy is given by $E_{\rm rm}^{\rm fix}(\mathrm{O}) - E^{\rm relax}$.

a local structure makes it easier for Si atoms to approach each other and form shorter Si–Si bonds, which is associated with the relaxation of neighboring bonding and ring networks after oxygen removal. By performing local stress calculations for an amorphous system that does not contain defects, it is possible to predict the sites where oxygen defects are likely to form without removing oxygen and relaxing the structure.

The local tensile stress is thought to be a local structure property that allows the interatomic distance to expand. For Si coincidence boundaries with well-defined atomic configurations, both theoretically and experimentally, bond stress of each Si–Si bond at the boundary-core region was calculated using the present scheme as a sum or average of the atomic stresses at both ends. The results revealed the presence of both tensile and compressive bond stresses [33]. Only for special boundaries with high rotation angles, high tensile stresses were observed for the reconstructed bonds at the core regions, indicating a high possibility of oxygen segregation at such bonds via oxygen insertion and the formation of Si–O–Si bonds. Experimentally, recent atom probe tomography (APT) experiments of the same coincidence boundaries in real polycrystalline Si ingots, combined with high-resolution electron microscopy observation, have provided the atomic-layer-scale oxygen concentration distribution at the boundary core regions [33]. APT of a specimen prepared by low-temperature focused ion beam (FIB) milling provided a one-dimensional (1D) proxigram concentration profile for oxygen across the $\Sigma 9\{114\}$ plane, which quantitatively revealed a segregation thickness of 2.5 nm. This profile was well reproduced by the 1D distribution of bond-centered sites under tensile stresses exceeding 1–2 GPa, determined from first-principles local stress calculations. The results showed the striking agreement between the high oxygen-concentration positions and the positions of special tensile bonds obtained by the present scheme. Moreover, these results indicate that the stress distribution of atomic groups can be used to identify local regions where chemical disorders such as defects and impurities occur in disordered structures.

It should be noted that the values of local energies and stresses inevitably depend on the chosen partitioning method. Nevertheless, the total sum of the partitioned local energies and the volume average of the partitioned local stresses are rigorously equal to the total energy and the cell stress of the supercell obtained by the conventional approach, ensuring the physical consistency of the analysis. At the same time, careful interpretation of such atomic quantities is required. Local energies depend explicitly on the local volumes as given in Eq. (2) and thus behave as extensive quantities. Conversely, local stresses, normalized by the local volumes as in Eq. (3), represent intensive quantities and are less affected by the partitioning scheme. In the present analysis, the local stress was further averaged over Si–O–Si units or SiO_4 units, which reduces the influence of the chosen partitioning method.

While the present study has focused on a-SiO_2, the same framework of analyzing local stress distributions can, in principle, be applied to other silica polymorphs as well as to other oxide glasses and related network–forming materials. In such systems, differences in local bond-angle flexibility and network topology are expected to manifest in distinct patterns of stress localization. There are, however, some important points to keep in mind when extending this approach. In the present work, when calculating the unit-averaged stress, we defined Eqs. (5) or (6) based on the fact that all Si atoms are fourfold coordinated and all O atoms are twofold coordinated. In other oxide glasses, the coordination numbers of cations and anions are often not constant. In such cases, the definition of the unit-averaged stress needs to be examined in more depth. Part of our possible future work will be to address this issue.

IV. CONCLUSIONS

In this study, we conducted a comprehensive first-principles investigation of the relationship between defect formation energies and local stress environments in a-SiO_2. By employing the real-space decomposition of stress via Bader analysis within the PAW–GGA framework and introducing unit-based averaging over local structural units, we successfully extended the applicability of local stress analysis from metals to disordered oxide systems.

Importantly, we found that the unit-averaged local stress within a Si–O–Si unit exhibits a strong inverse correlation with the formation energy of an oxygen vacancy (correlation coefficient 0.91), indicating that oxygen atoms in a locally compressive environment are more likely to form vacancies with large structural relaxation. Furthermore, we demonstrate that this correlation allows us to predict possible vacancy sites directly from a nondefective structure without the need to explicitly relax the vacancy configurations. This represents a significant reduction in computational cost and effort, particularly for amorphous models with large structural variation. These results provide insights into the defect formation mechanism in oxide glasses and establish a practical computational approach for identifying weak atomic sites based solely on the local stress field. The proposed approach is expected to accelerate defect analysis and material optimization in disordered and ionic systems.

ACKNOWLEDGMENTS

This work was supported by a MEXT KAKENHI grant awarded to T.T. (Grants No. 23K23076 and No. 25K01856) and partially supported by CNRS through the International Research Project (IRP) "Functional inorganic materials for global social challenges" labeled FRESH.

The manuscript was written through contributions of all authors. All authors have approved the final version of the manuscript. K.M.: data curation, formal analysis, visualization, and writing—original draft; T.I.: data curation and formal analysis; T.T.: conceptualization, methodology, and writing—review and editing; S.T.: methodology; M.K.: methodology and writing—review and editing; A.B.: conceptualization.

DATA AVAILABILITY

The data that support the findings of this article are not publicly available upon publication because it is not technically feasible and/or the cost of preparing, depositing, and hosting the data would be prohibitive within the terms of this research project. The data are available from the authors upon reasonable request.

[1] L. Skuja, M. Hirano, H. Hosono, and K. Kajihara, Defects in oxide glasses, Phys. Status Solidi C **2**, 15 (2005).

[2] K. Raghavachari, D. Ricci, and G. Pacchioni, Optical properties of point defects in SiO_2 from time-dependent density functional theory, J. Chem. Phys. **116**, 825 (2002).

[3] H. Hosono, Y. Ikuta, T. Kinoshita, K. Kajihara, and M. Hirano, Physical disorder and optical properties in the vacuum ultraviolet region of amorphous SiO_2, Phys. Rev. Lett. **87**, 175501 (2001).

[4] L. Skuja, Optically active oxygen-deficiency-related centers in amorphous silicon dioxide, J. Non-Cryst. Solids **239**, 16 (1998).

[5] T. Tamura, S. Ishibashi, S. Tanaka, M. Kohyama, and M. H. Lee, First-principles analysis of the optical properties of structural disorder in SiO_2 glass, Phys. Rev. B **77**, 085207 (2008).

[6] R. A. Weeks and C. M. Wilson, Irradiation effects and short-range order in fused silica and quartz, J. Appl. Phys. **31**, 1555 (1960).

[7] R. A. Weeks, The many varieties of E' centers: A review, J. Non-Cryst. Solids **179**, 1 (1994).

[8] G. I. Csonka and J. Réffy, Density functional study of the equilibrium geometry and Si–O–Si potential energy curve of disiloxane, Chem. Phys. Lett. **229**, 191 (1994).

[9] A. T. Hanindriyo, A. K. S. Yadav, T. Ichibha, R. Maezono, K. Nakano, and K. Hongo, Diffusion Monte Carlo evaluation of disiloxane linearisation barrier, Phys. Chem. Chem. Phys. **24**, 3761 (2022).

[10] B. Jia, Z. Guan, Z. Peng, J. Zhang, X. Guan, P. Guan, B. Yang, Y. Wang, and P. Lu, Structural disorder in fused silica with ODC(I) defect, Appl. Phys. A **124**, 696 (2018).

[11] G. Kresse and J. Furthmüller, Efficient iterative schemes for *ab initio* total-energy calculations using a plane-wave basis set, Phys. Rev. B **54**, 11169 (1996).

[12] G. Kresse and D. Joubert, From ultrasoft pseudopotentials to the projector augmented-wave method, Phys. Rev. B **59**, 1758 (1999).

[13] S. J. Clark, M. D. Segall, C. J. Pickard, P. J. Hasnip, M. I. J. Probert, K. Refson, and M. C. Payne, First principles methods using CASTEP, Z. Kristallogr. **220**, 567 (2005).

[14] A. H. Romero, D. C. Allan, B. Amadon, G. Antonius, T. Applencourt, L. Baguet, J. Bieder, F. Bottin, J. Bouchet, E. Bousquet *et al.*, ABINIT: Overview and focus on selected capabilities, J. Chem. Phys. **152**, 124102 (2020).

[15] P. Giannozzi, S. Baroni, N. Bonini, M. Calandra, R. Car, C. Cavazzoni, D. Ceresoli, G. L Chiarotti, M. Cococcioni, I. Dabo *et al.*, QUANTUM ESPRESSO: A modular and open-source software project for quantum simulations of materials, J. Phys.: Condens. Matter **21**, 395502 (2009).

[16] P. Giannozzi, O. Andreussi, T. Brumme, O. Bunau, M. B. Nardelli, M. Calandra, R. Car, C. Cavazzoni, D. Ceresoli, M. Cococcioni *et al.*, Advanced capabilities for materials with QUANTUM ESPRESSO, J. Phys.: Condens. Matter **29**, 465901 (2017).

[17] Y. Shiihara, M. Kohyama, and S. Ishibashi, *Ab initio* local stress and its application to Al (111) surfaces, Phys. Rev. B **81**, 075441 (2010).

[18] H. Wang, M. Kohyama, S. Tanaka, and Y. Shiihara, *Ab initio* local energy and local stress: Application to tilt and twist grain boundaries in Cu and Al, J. Phys.: Condens. Matter **25**, 305006 (2013).

[19] J. P. Perdew, K. Burke, and M. Ernzerhof, Generalized gradient approximation made simple, Phys. Rev. Lett. **77**, 3865 (1996).

[20] P. E. Blöchl, Projector augmented-wave method, Phys. Rev. B **50**, 17953 (1994).

[21] S. Ishibashi, T. Tamura, S. Tanaka, M. Kohyama, and K. Terakura, *Ab initio* calculations of electric-field-induced stress profiles for diamond/*c*-BN (110) superlattices, Phys. Rev. B **76**, 153310 (2007).

[22] N. Chetty and R. M. Martin, First-principles energy density and its applications to selected polar surfaces, Phys. Rev. B **45**, 6074 (1992).

[23] A. Filippetti and V. Fiorentini, Electrostatics and polarization in bulk insulators and dielectrics: First-principles theory and applications, Phys. Rev. B **61**, 8433 (2000).

[24] M. Kohyama, S. Tanaka, and Y. Shiihara, *Ab initio* local-energy and local-stress calculations for materials science and engineering, Mater. Trans. **62**, 1 (2021).

[25] T. Tamura, M. Karasuyama, R. Kobayashi, R. Arakawa, Y. Shiihara, and I. Takeuchi, Fast and scalable prediction of local energy at grain boundaries: Machine-learning-based modeling of first-principles calculations, Modelling Simul. Mater. Sci. Eng. **25**, 075003 (2017).

[26] T. Tamura and M. Karasuyama, Prediction of formation energies of large-scale disordered systems via active-learning-based executions of *ab initio* local-energy calculations, Phys. Rev. Mater. **4**, 113602 (2020).

[27] I. T. Todorov, W. Smith, K. Trachenko, and M. T. Dove, DL_POLY_3: New dimensions in molecular dynamics simulations via massive parallelism, J. Mater. Chem. **16**, 1911 (2006).

[28] S. Nosé, A unified formulation of the constant temperature molecular dynamics methods, J. Chem. Phys. **81**, 511 (1984).

[29] A. Pedone, G. Malavasi, M. C. Menziani, A. N. Cormack, and U. Segre, A new self-consistent empirical interatomic potential model for oxides, silicates, and silica-based glasses, J. Phys. Chem. B **110**, 11780 (2006).

[30] M. Yu, D. R. Trinkle, and R. M. Martin, Accurate and efficient algorithm for bader charge integration, Phys. Rev. B **83**, 115113 (2011).

[31] T. Tamura, S. Tanaka, and M. Kohyama, Full-PAW calculations of XANES/ELNES spectra of ti-bearing oxide crystals and TiO-SiO glasses: Relation between pre-edge peaks and Ti coordination, Phys. Rev. B **85**, 205210 (2012).

[32] N. Richard, S. Girard, L. Martin-Samos, V. Cuny, A. Boukenter, Y. Ouerdane, and J.-P. Meunier, First principles study of oxygen-deficient centers in pure and Ge-doped silica, J. Non-Cryst. Solids **357**, 1994 (2011).

[33] Y. Ohno, J. Ren, S. Tanaka, M. Kohyama, K. Inoue, Y. Shimizu, Y. Nagai, and H. Yoshida, Insight into segregation sites for oxygen impurities at grain boundaries in silicon, Appl. Phys. Express **14**, 041003 (2021).